Electronic Supplementary Information

1,2,4-Triazolium perfluorobutanesulfonate as an archetypal pure protic organic ionic plastic crystal electrolyte for all-solid-state fuel cells

Jiangshui Luo,*[a,b] Annemette H. Jensen,[c] Neil R. Brooks,[d] Jeroen Sniekers,[d] Martin Knipper,[e] David Aili,[c] Qingfeng Li,*[c] Bram Vanroy,[f] Michael Wübbenhorst,[f] Feng Yan,[g] Luc Van Meervelt,[d] Zhigang Shao,[h] Jianhua Fang,[i] Zheng-Hong Luo,[i] Dirk E. De Vos,*[b] Koen Binnemans*[d] and Jan Fransaer*[a]

[a] *Department of Materials Engineering, KU Leuven, Leuven 3001, Belgium. Fax: +32 16 3 21990; Tel: +32 16 32 12 39; E-mail: jan.fransaer@mtm.kuleuven.be*
[b] *Centre for Surface Chemistry and Catalysis, KU Leuven, Leuven 3001, Belgium. Fax: +32 16 3 21998; E-mail: dirk.devos@biw.kuleuven.be; jiangshui.luo@biw.kuleuven.be;*
[c] *Department of Energy Conversion and Storage, Technical University of Denmark, Kgs. Lyngby 2800, Denmark. Fax: +45 45 88 31 36; Tel: +45 45 25 23 18; E-mail: qfli@dtu.dk*
[d] *Department of Chemistry, KU Leuven, Leuven 3001, Belgium. Fax: +32 16 3 27992; Tel: +32 16 32 74 46; E-mail: koen.binnemans@chem.kuleuven.be*
[e] *Department of Physics, University of Oldenburg, Oldenburg 26129, Germany.*
[f] *Department of Physics and Astronomy, KU Leuven, Leuven 3001, Belgium.*
[g] *Department of Polymer Science and Engineering, Soochow University, Suzhou 215123, China.*
[h] *Dalian Institute of Chemical Physics, Chinese Academy of Sciences, Dalian 116023, China.*
[i] *School of Chemistry and Chemical Engineering, Shanghai Jiao Tong University, Shanghai 200240, China.*

Table of Contents

Section 1*: *Supplementary Experiments ·····3

Section 2: Supplementary Infrared, Thermal and Structural Analysis·····4

Section 3: Supplementary Figures·····8

S1: FT-IR spectrum of powders of compound **1**·····8

S2: Raman spectra of **1** in the form of a pressed thin-film pellet and 1*H*-1,2,4-triazole in the form of a plate at 30 ℃·····8

S3: Thermogravimetric analysis (TGA) of **1** recorded in a nitrogen atmosphere·····9

S4: TGA trace of **1** recorded an air atmosphere·····9

S5: Polarized optical microscopic images for powders of compound **1**·····10

S6: DSC curves of a dense pellet of **1** at a heating/cooling rate of 2 ℃ min^{-1}·····11

S7: DSC curves of fine powders of **1** at a heating/cooling rate of 2 ℃ min^{-1}·····11

S8: SEM images of a plate formed by natural solidification of melts of **1** in air·····12

S9: Powder XRD patterns of a pressed pellet and fine powders of **1** at 25 ℃·····13

S10: Powder XRD patterns of a pressed pellet and fine powders of **1** at 160 ℃·····14

S11: View of the crystal structure of **1** showing the hydrogen bonds between one 1,2,4-triazolium cation and three neighbouring perfluorobutanesulfonate anions·····15

S12: View of the packing in the crystal structure of **1** at 27 ℃·····16

S13: Variable-temperature FT-IR spectra of **1** between 82 ℃ and 190 ℃·····17

S14: FT-IR spectrum of 1-methylimidazolium perfluorobutanesulfonate·····18

S15: FT-IR spectrum of 1,2,4-triazolium benzenesulfonate·····19

S16: Images of the crystal recorded during variable-temperature FT-IR measurements·····21

S17: The evolution of the optical microscopic images of the sample when the temperature reached 165 ℃ for 4, 7, 9, 11, 15, and 20 min·····22

S18: Temperature-dependent powder XRD patterns of powders of **1** from 160 ℃ to 185 ℃·····23

S19: OCV at 25 ℃ versus time for a fuel cell with a pellet of powders of **1** as the electrolyte·····24

Section 4*: *Supplementary Table

Table S1: Fitting slopes of the polarization curves shown in Fig. 14a·····25

Section 5*: *Supplementary Movie

Movie S1: The plastic flow of a crystal at t = ~3 min when it was heated at 165 ℃·····26

References·····26

Section 1: Supplementary Experiments

NMR analysis

^{1}H NMR (400 MHz, DMSO-d_6): δ 9.33 (s, 2H, C−H), δ 14.3 (s, 2H, N−H). ^{13}C NMR (100 MHz, DMSO-d_6): δ 143.16, δ 39.39.

Temperature-dependent powder XRD patterns for a pressed cylindrical dense pellet:

Temperature-dependent powder XRD patterns for a pressed cylindrical dense pellet of **1** was recorded in an argon atmosphere from 25 ℃ to 160 ℃ on a powder X-ray diffractometer (X'Pert PRO, PANalytical) using Cu Kα radiation (λ = 1.5406 Å). The cylindrical dense pellet was prepared by uniaxial pressing of fine powders of **1** in a 10 mm diameter metal die under 20 kN (corresponding to a pressure of 255 MPa) for 1 min. Measurements were done in a high-temperature oven chamber (HTK 1200N, Anton Paar) using a coin-like metal sample holder. The heating element installed is a Kanthal APM (Cr: 22%; Al: 5.8%; Fe: rest) and the thermocouple is a Pt-10%Rh-Pt sensor (type S). The sample was stabilized at each measurement temperature (accuracy: ±1 ℃) for about 20 min before each measurement. The temperature ramp between two consecutive temperatures was 2 ℃ min^{-1}. Each measurement consisted of a θ–2θ scan from 10 ° to 50 ° with a step size of 0.052 ° and a scan speed of 0.039 °s^{-1}.

Comparison of moisture absorbing property:

Certain amounts of **1** and 85% H_3PO_4 were weighed in dry and clean beakers and then placed on a dry plate in a closed pot with plenty of water filled at the bottom of the pot to compare the respective gain of weight at room temperature after 48 h. The air in the closed system could be considered nearly fully humid. It was found that **1** was not hygroscopic without detectable gain of weight (accuracy of the balance used: ± 0.1 mg) while 85% H_3PO_4 showed obvious increase of weight ($\Delta m/m \times 100\%$ = $\frac{2.3344\ \text{g}}{23.8365\ \text{g}} \times 100\% = 9.79\%$) indicating its strong moisture absorbing property.

Section 2: Supplementary Infrared, Thermal and Structural Analysis

Infrared analysis

The absence of both of the O−H stretching bands between 3400 and 3800 cm^{-1} and the H−O−H bending band at around 1650 cm^{-1} in the FT-IR spectrum (Fig. S1) confirms the very low water content of **1**.[S1−S3] The ultra-low water content may also be further indicated by the material's ultra-low ionic conductivity of 3.21×10^{-10} S cm^{-1} at 65 ℃ in the ordered crystalline state (Fig. 11). The bands at 3230, 3163 and 2941 cm^{-1} are associated with N−H stretching.[S4,S5] The peak at 3136 cm^{-1} is attributed to the C−H stretch of the triazole ring.[S6] In addition, the bands at 1533 and 943 cm^{-1} are assigned to the ring stretching and N−H out-of-plane bending of the 1,2,4-triazolium cations, respectively.[S6] The peaks at 1354, 1262, 1221, 1193, 1165, 1138, 1064, 1040, 1023, 903, 805, 740 and 659 cm^{-1} are associated with the $CF_3(CF_2)_3SO_3^-$ anions.[S7−S11] For instance, the sharp absorption bands at around 1262 and 1193 cm^{-1} may correspond to the SO_3 asymmetric stretching vibration.[S7,S8] This spectral feature is characteristic for a sulfonate anion strongly involved in a hydrogen bond.[S9] The peaks at 1064, 1040 and 1023 cm^{-1} are attributed to the SO_3 symmetric stretching vibration of sulfonate anions.[S7,S10] The peak at 1221 cm^{-1} may be due to the perfluorobutyl functional groups of **1**.[S7,S11]

Thermal analysis

The relatively large $\Delta S_{III\rightarrow II}$ of 26.0 J K^{-1} mol^{-1} (Fig. 3) implies that the ions in **1** have a large extent of orientational freedom in Phase II. Assuming that the configurational entropy is the most dominant contribution for solid-solid phase transitions, the entropy change can be approximated according to Equation (S1):

$$\Delta S = \mathrm{R} \times \ln(n_1 / n_2) \quad \text{(S1)}$$

where R is the universal gas constant (8.314 J mol^{-1} K^{-1}), and n_1/n_2 is the ratio of the number of orientational freedoms of constituent molecules in the high and low temperature phases, respectively.[S12,S13] A ratio of 22.8 is obtained for $\Delta S_{III\rightarrow II}$ and this value is considered to account for the change in the number of orientations of all ions at $T_{III\rightarrow II}$. Moreover, compared with imidazolium

methanesulfonate (T_{mp} = 188 ℃, $T_{II\rightarrow I}$ = 174 ℃),[S14] **1** exhibits a similar melting point but a much lower solid-solid phase transition temperature ($T_{III\rightarrow II}$ = 76.8 ℃, $T_{II\rightarrow I}$ = 87.2 ℃).

During the cooling scan, three corresponding exothermic peaks were recorded in the DSC trace (Fig. 3). Firstly, **1** crystallizes at around 176.8 ℃ with a sudden release of latent heat, which is similar to some reported plastic crystals.[S15,S16] The crystallization results in a slightly increased sample temperature in the dynamic DSC experiment as a loop in the cooling curve is seen at the crystallization temperature. Furthermore, each of the two reversible heat anomalies at 76.8 ℃/47.2 ℃ and 87.2 ℃/86.6 ℃ (on heating/cooling) displays a well-shaped peak on the DSC curve and a temperature hysteresis, proving the transformations of phase III → phase II and phase II → phase I are both first-order solid-solid phase transitions.[S17] DSC tests of **1** in the form of a pressed dense pellet (Fig. S6) or at a lower heating/cooling rate of 2 ℃ min^{-1} for fine powders (Fig. S7) are consistent with the DSC traces for fine powders of **1** recorded at 5 ℃ min^{-1} (Fig. 3).

Variable-temperature powder XRD analysis

To characterize the low temperature transitions at 76.8 ℃ and 87.2 ℃ as shown in the DSC trace (Fig. 3), fine powders of **1** were heated from 25 ℃ to 160 ℃ and the structural features were monitored by temperature-dependent powder XRD. As shown in Fig. 4, several diffraction peaks disappear or appear during the two endothermic transitions. When the sample was heated from 25 ℃ to 73 ℃, the powder XRD patterns were basically the same. From 74 ℃ to 78 ℃, two large reflections at 2θ = 17.9 ° and 23.8 ° as well as some minor reflections at 2θ = 11.4 °, 12.5 °, 14.2 °, 16.2 °, 18.5 °, 22.7 °, 27.6 °, 33.9 °, 34.6 °, 37.5 ° and 43.6 ° become weaker and disappear completely before 77 ℃ or 78 ℃. In particular, two major reflections at 2θ = 29.7 ° and 35.8 ° diminish quickly and disappear completely at around 80 ℃, indicating clearly a transformation between two different crystalline structures and a likely increase in space group symmetry. These changes confirm the first endothermic transition (phase III → phase II), whose onset temperature is 76.8 ℃ and peak temperature is 78.4 ℃, to be a solid−solid phase transition. This phase transition is accompanied by an evident entropy change, $\Delta S_{III\rightarrow II}$, of 26.0 J K^{-1} mol^{-1}.

Meanwhile, starting from 74 ℃, several new reflections emerge at 2θ = 13.8 °, 16 ° and 19.5 ° and grow sharper and stronger at 85 ℃ while the weak diffraction peaks at 2θ = 17.4 ° and 32.3 ° vanish at about 82 ℃. From 81 ℃ to 85 ℃, obvious diffraction peaks at 2θ = 21.9 °, 27.4 ° and 32.9 ° begin to arise. In addition, weak diffraction peaks at 2θ = 16.5 °, 16.7 ° and 29.3 ° begin to appear at 82 ℃. From 85 ℃ to 160 ℃, the powder XRD patterns of the sample remain almost the same except a gradual shift in the peak positions toward lower 2θ values with increasing temperature due to continuous minor structural changes (*i.e.* thermal expansion of the lattice). Therefore, the second endothermic transition (phase II → phase I) at 87.2 ℃ in the heating scan of DSC trace is proved to be another solid−solid phase transition, though with a smaller entropy change, $\Delta S_{\mathrm{II}\rightarrow\mathrm{I}}$, of 5.35 J K^{-1} mol^{-1}. The slight difference in onset temperatures of lattice transformation and thermal transition should be related to the different heating methods for powder XRD and DSC measurements.[S14] The sharp reflections suggest that **1** possess long-range-ordered structures in phase I, II and III. While all of the diffraction peaks belong to the room temperature (phase III) powder XRD pattern completely disappear in phase I (the highest temperature solid phase), the powder XRD patterns of phase I are observed to be simpler, implying a more symmetric lattice system and phase I as a plastic phase.[S12,S14,S15,S17−S23] The reduction of diffraction peaks in phase I indicates the presence of dynamic rotational disorder which leads to the plastic properties. In addition, the increased rotating motion of ions increases the thermal factors of the atoms in the lattice and prevents diffraction in the high-2θ-angle region (e.g., 2θ > 35 ° above 82 ℃ as shown in Fig. 4).[S23]

Furthermore, Fig. S9 compares the powder XRD patterns of a pressed cylindrical dense pellet and fine powders of compound **1** at 25 ℃. The pellet was formed by uniaxial pressing of fine powders. While the fine powders show relatively clear and well resolved Bragg reflections with a weak diffuse background, the dense pellet shows an increase in intensity of the diffuse scattering background and an alteration in peak intensities, which might indicate the disorder.[S24,S25] When the temperature goes up to 160 ℃ (Fig. S10), the fine powders exhibit disorder as evidenced by the amorphous type diffraction which underlies the peaks.[S24] Meanwhile, the pellet displays simpler powder XRD patterns (*vs*. Fig. S9a and S10b) with remarkable alteration in peak intensities and some peaks

missing, again suggesting stronger rotational disorder in the plastic phase (phase I), which corresponds to the increased ionic conductivity (Fig. 11).

Single-crystal XRD analysis

The geometry of the anion (Fig. 7) is not linear as one may expect for a *n*-butyl chain as can be seen by the torsion angles along the chain (e.g., S6−C10−C13−C16 = −162.1(2)° at −173 ℃ and −170.5(6) °at 27 ℃; C10−C13−C16−C19 = −162.6(3)° at −173 ℃ and −174.6(12) °at 27 ℃).

It was also attempted to record single-crystal XRD data above 27 ℃ and above the transition temperatures of phase III → phase II and phase II → phase I. Above 27 ℃, the thermal motion of the perfluorobutyl chains increased further and made the structure refinements of very poor quality. Above the transition temperature of phase III → phase II, it was evident that the recorded diffraction patterns were no longer of single crystals so no structural information could be obtained.

Section 3: Supplementary Figures

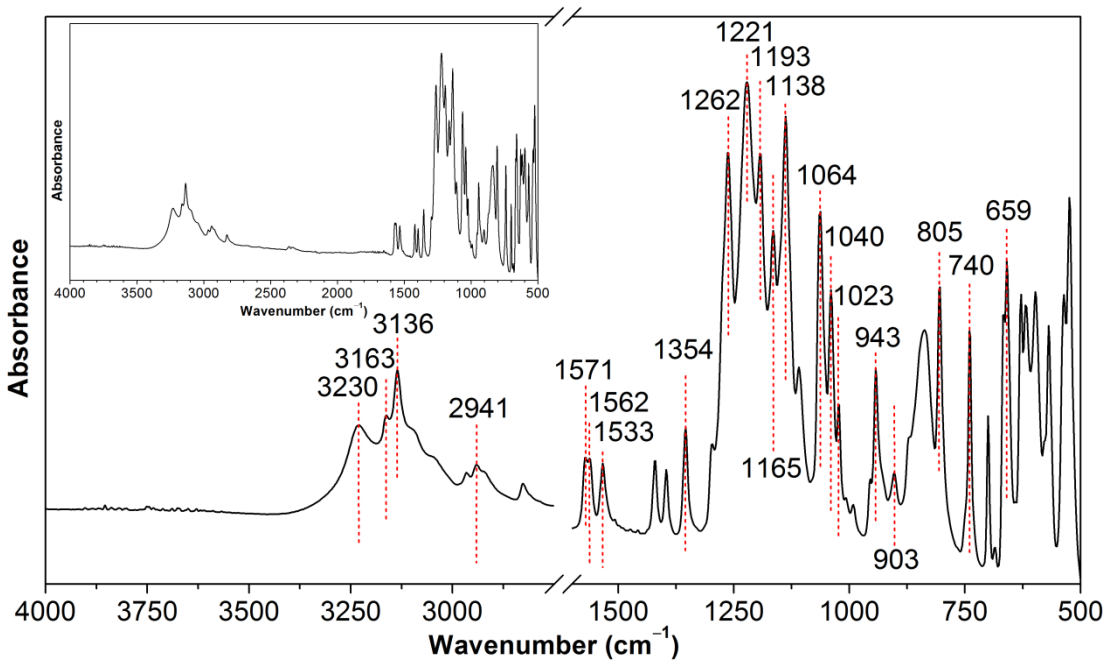

Fig. S1. FT-IR spectrum of powders of compound **1** recorded on a Bruker VERTEX 70 FT-IR spectrometer with an ATR accessory at room temperature. The inset is the complete IR spectrum, showing the absence of the H−O−H bending band of water at ~1650 cm^{-1}.

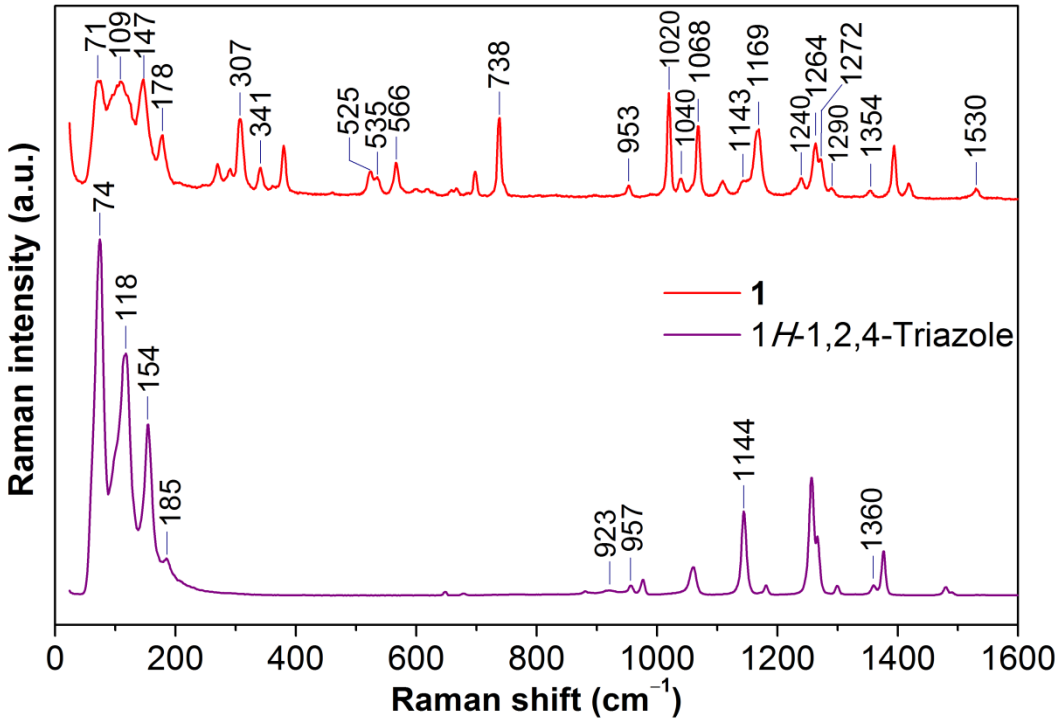

Fig. S2. Raman spectra of **1** in the form a pressed thin-film pellet (top curve) and 1*H*-1,2,4-triazole in the form of a plate (bottom curve) at 30 ℃. Data were recorded on a WITec Project system using a 785 nm excitation laser line. No traces of 1*H*-1,2,4-triazole have been detected in the Raman spectrum of **1**.

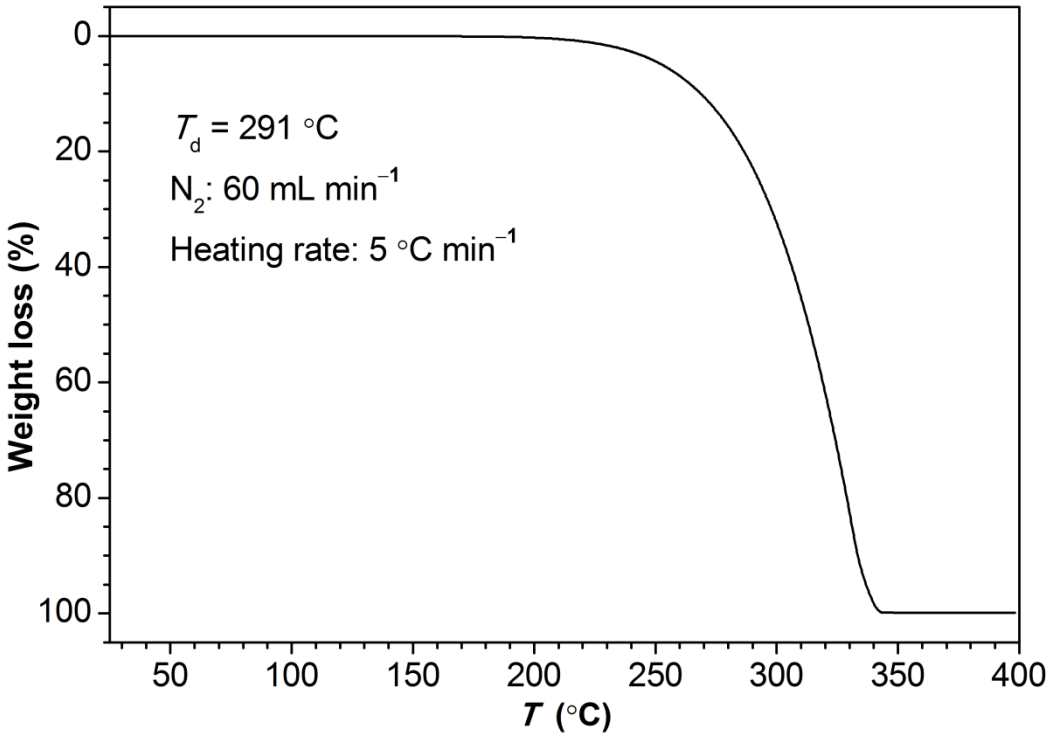

Fig. S3. Thermogravimetric analysis (TGA) of **1** recorded in a nitrogen atmosphere (60 mL min^{-1}) at a heating rate of 5 ℃ min^{-1}. The onset temperature of weight loss was used as the decomposition temperature (T_d). The one-step weight loss process also confirms the high purity of **1**.

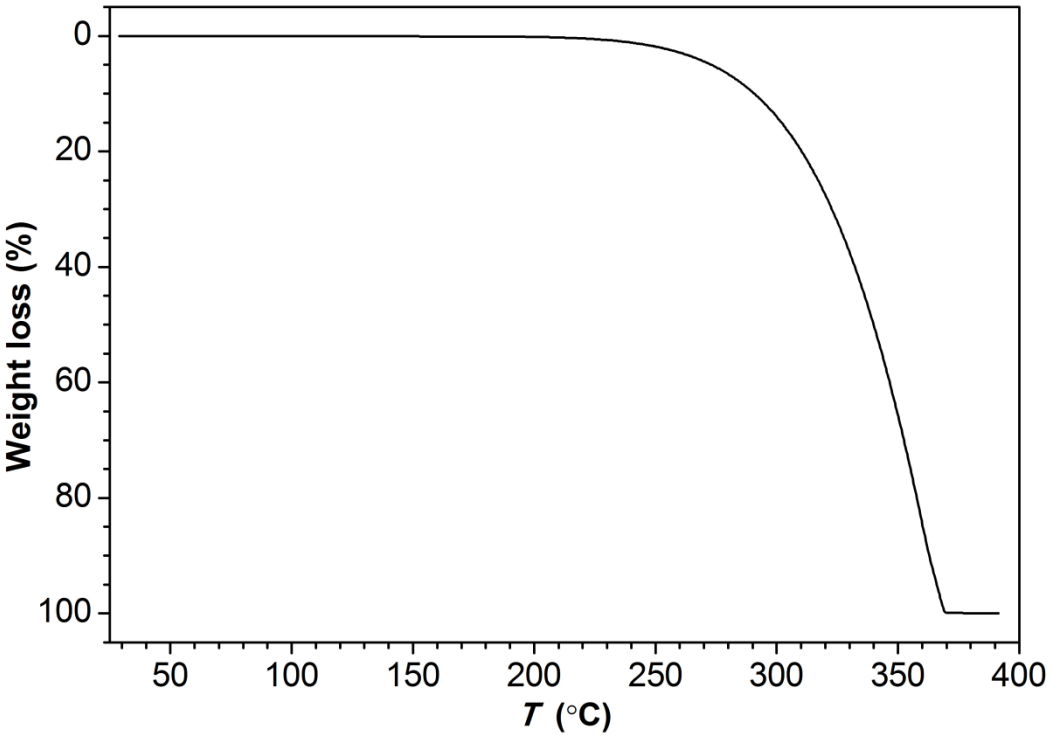

Fig. S4. TGA trace of **1** recorded in an air atmosphere (60 mL min^{-1}) at a heating rate of 10 ℃ min^{-1}, indicating that compound **1** is thermally stable in air.

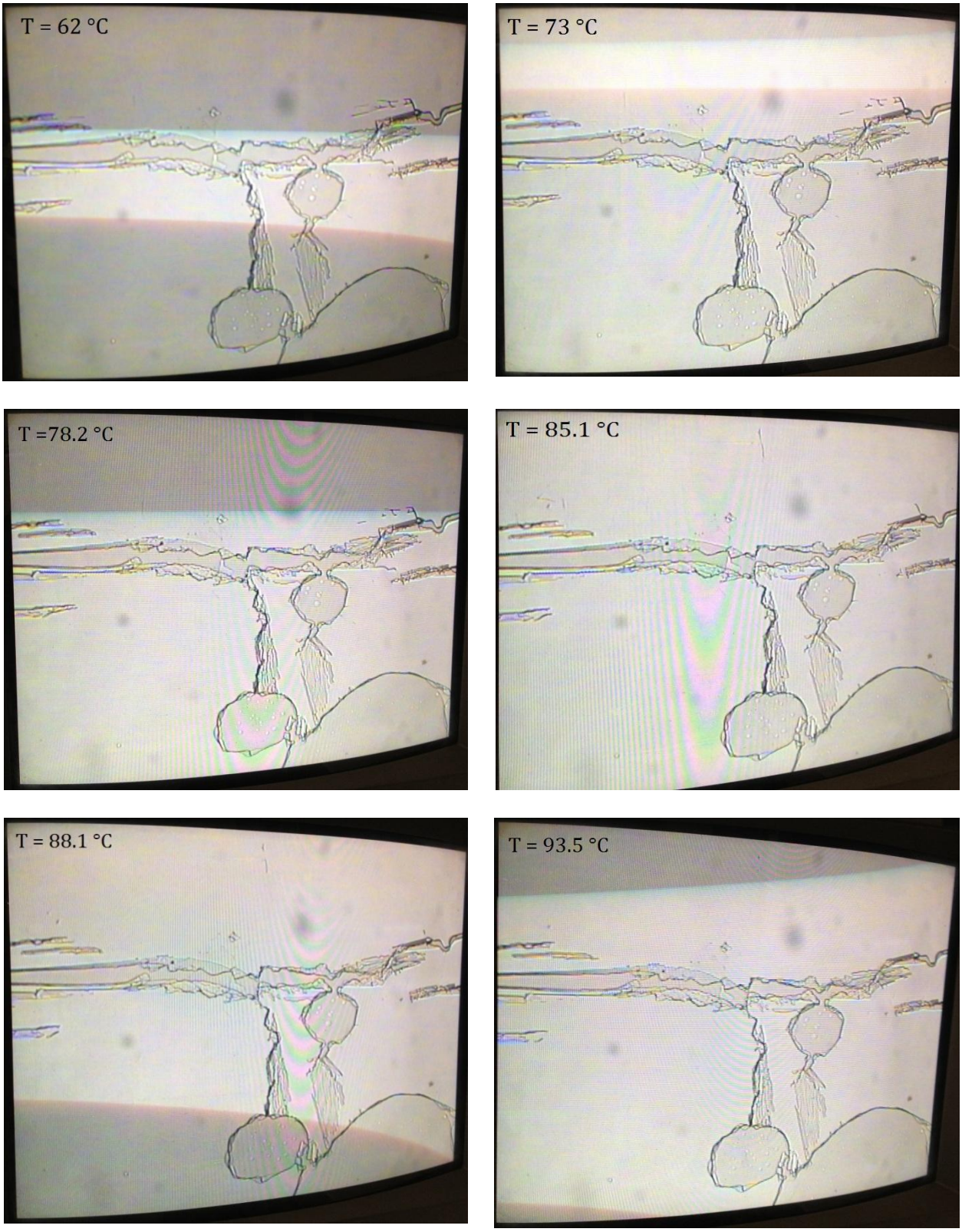

Fig. S5. Polarized optical microscopic images for powders of compound **1** placed between two glass plates during reheating from room temperature (phase III) to phase I, excluding the possibility of partial melting of **1** at around 77 ℃ and 87 ℃. The heating rate was 10 ℃ min^{-1}. Pictures were taken of the instant images shown on a Sony Trinitron monitor by using an iPhone 4S camera.

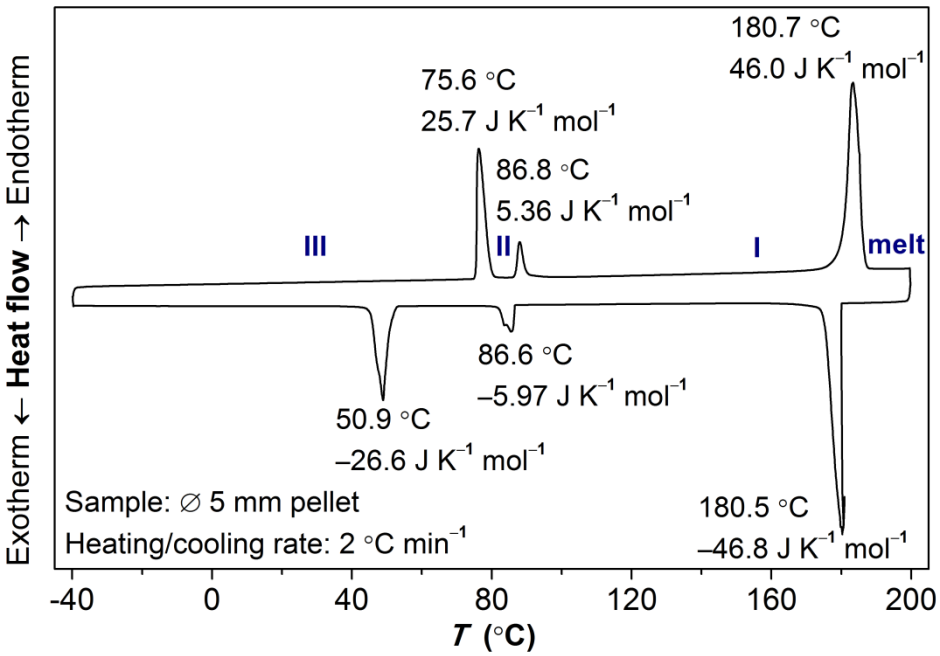

Fig. S6. DSC curves of **1** in the form of a pressed dense pellet with a diameter of 5 mm (sample mass: 45.37 mg). The onset temperatures and entropy changes for each phase transition are given. The heating/cooling rate was 2 ℃ min^{-1}. *The pellet is expected to have better contact with aluminum hermetic pans during DSC measurements than fine powders.* The sudden release of latent heat during the solidification is also seen for **1** in the form of a pressed dense pellet.

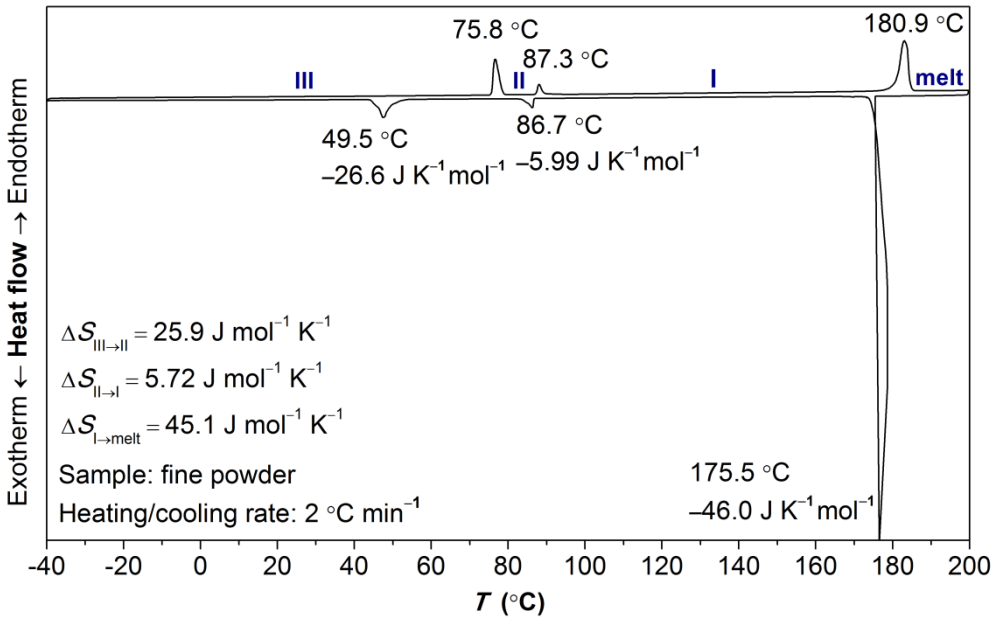

Fig. S7. DSC curves of **1** in the form of fine powders (sample mass: 19.47 mg) at a heating/cooling rate of 2 ℃ min^{-1}. The onset temperatures and entropy changes for each phase transition are given. Similar to **Fig. 3** and **Fig. S6**, the sudden release of latent heat during the solidification is also seen for **1** at a lower cooling rate. Again, the crystallization results in a slightly increased sample temperature in the dynamic DSC experiment as a loop in the cooling curve is seen at the crystallization temperature.

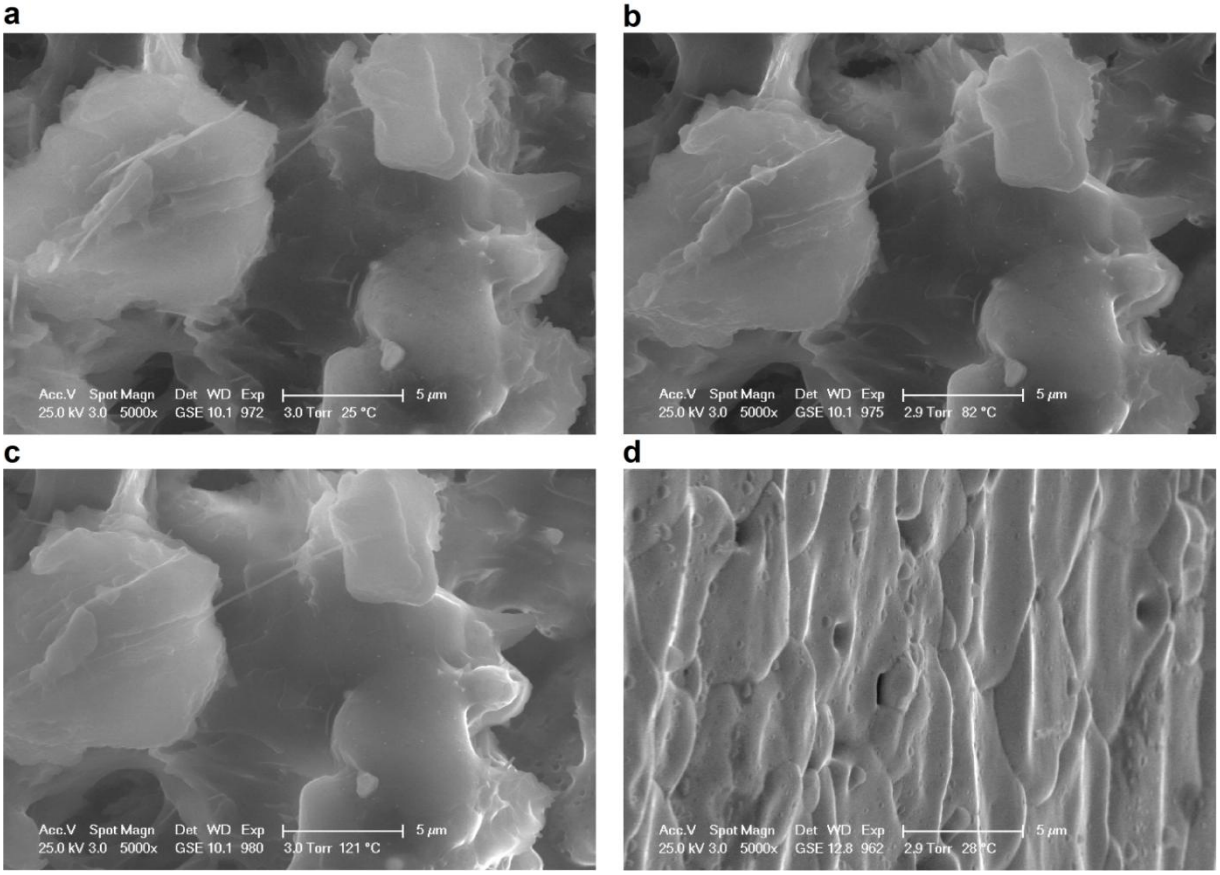

Fig. S8. SEM images of a plate, which was formed by natural solidification of melts of **1** in air. Images were acquired at different temperatures under a vacuum of around 3.0 Torr (*i.e.* ~400 Pa) with an acceleration voltage of 25.0 kV. Slip planes and steps on the fracture of the plate at (a) 25 ℃, (b) 82 ℃ and (c) 121 ℃, corresponding to phase III, II and I, respectively. (d) Slip planes appearing at the surface of the plate at 28 ℃. The holes are probably due to gas bubbles.

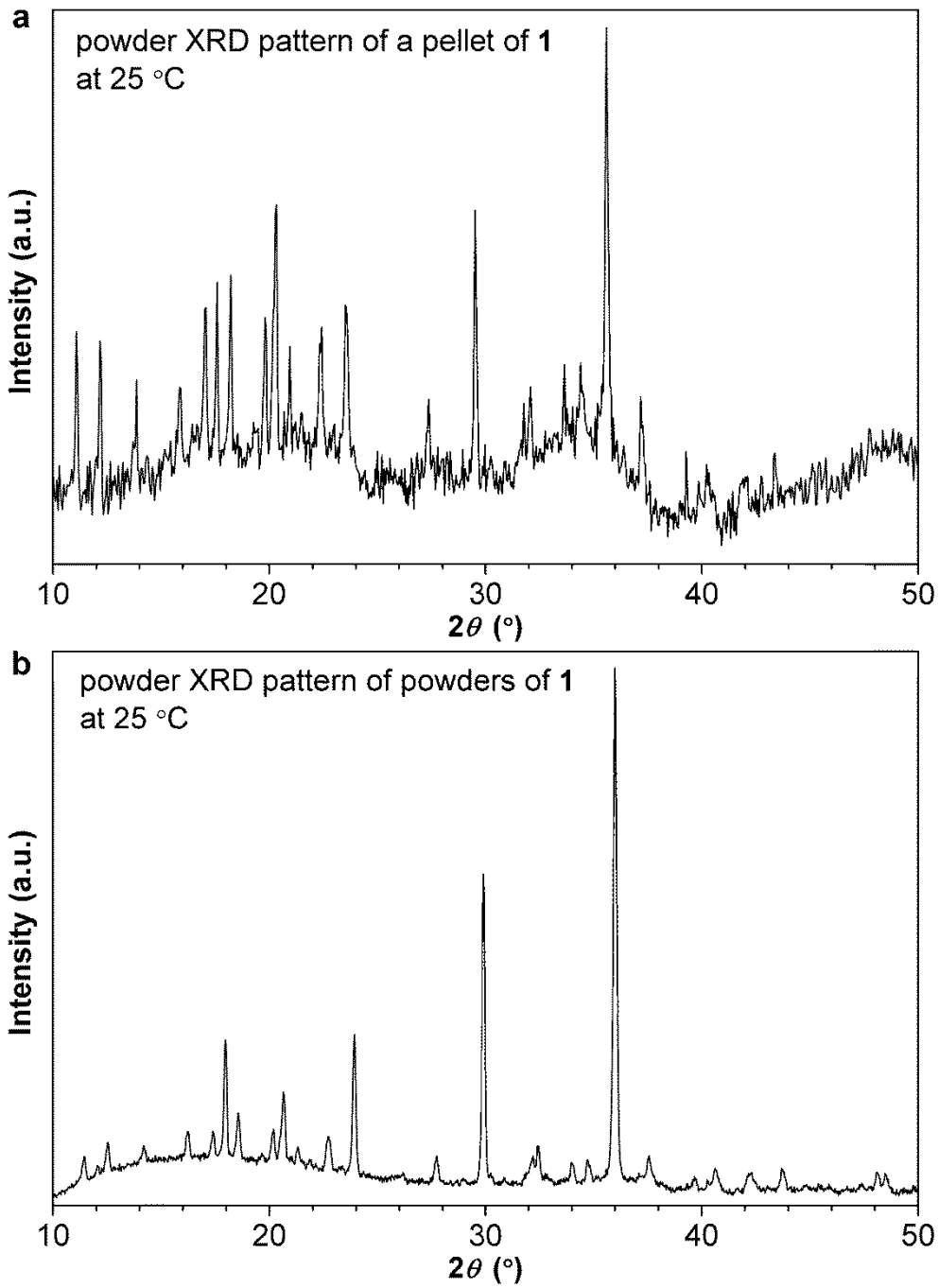

Fig. S9. Powder XRD patterns of (a) a pressed cylindrical dense pellet and (b) fine powders of compound **1** at 25 ℃. The cylindrical dense pellet was prepared by uniaxial pressing of fine powders of **1** in a 10 mm diameter metal die under 20 kN (corresponding to a pressure of 255 MPa) for 1 min. Measurements were done in a high-temperature oven chamber (HTK 1200N, Anton Paar) with Ar atmosphere. The overall shift to higher 2θ values (also in **Fig. S10**) for peak positions of fine powders compared with those of the pressed dense pellet is most likely due to the error of height adjustment before measurement. The same X-ray diffractometer (X'Pert PRO, PANalytical) using Cu Kα radiation (λ = 1.5406 Å) was employed. Measurements were done in the same high-temperature oven chamber (HTK 1200N, Anton Paar) with argon atmosphere. Step size: (a) 0.052 °; (b) 0.026 °. Scan speed: (a) 0.039 °s^{-1}; (b) 0.011 °s^{-1}.

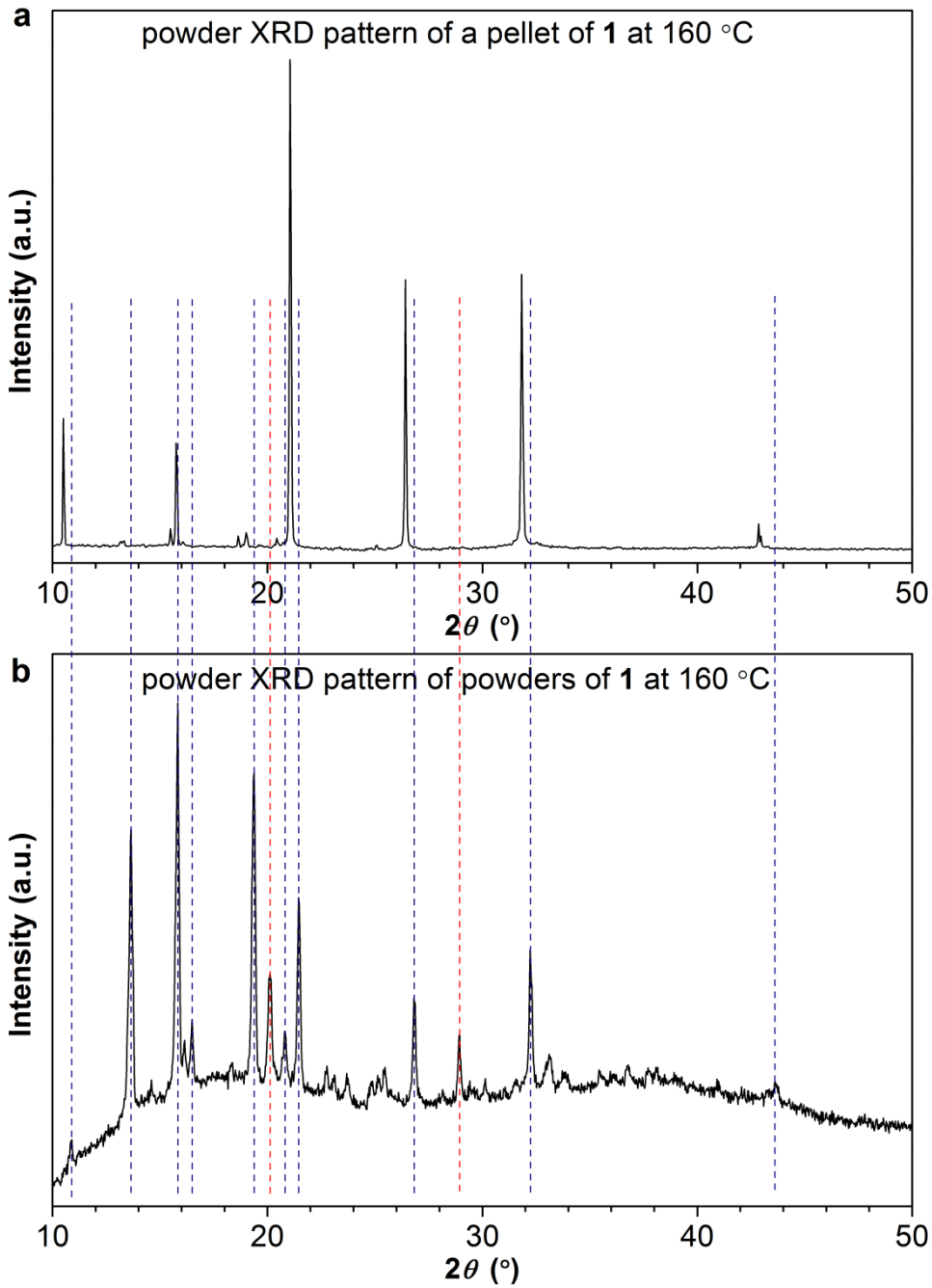

Fig. S10. Powder XRD patterns of (a) a pressed cylindrical dense pellet and (b) fine powders of compound **1** at 160 ℃ after the measurements at 25 ℃ shown in **Fig. S9**. The overall shift to higher 2θ values for peak positions of fine powders compared with those of pressed pellet is most likely due to the error of height adjustment before the measurement. It is clear that the reflections of fine powders of **1** include all of those of the pressed dense pellet of **1** with remarkable alteration in peak intensities and even some peaks missing (marked by red dashed line) in the latter. The fine powders exhibit disorder as evidenced by the broad amorphous type diffraction which underlies the peaks. The same X-ray diffractometer (X'Pert PRO, PANalytical) with Cu Kα radiation (λ = 1.5406 Å) was used. Measurements were done in the same high-temperature oven chamber (HTK 1200N, Anton Paar) with argon atmosphere. Step size: (a) 0.052 °; (b) 0.026 °. Scan speed: (a) 0.039 ° s^{-1}; (b) 0.011 ° s^{-1}.

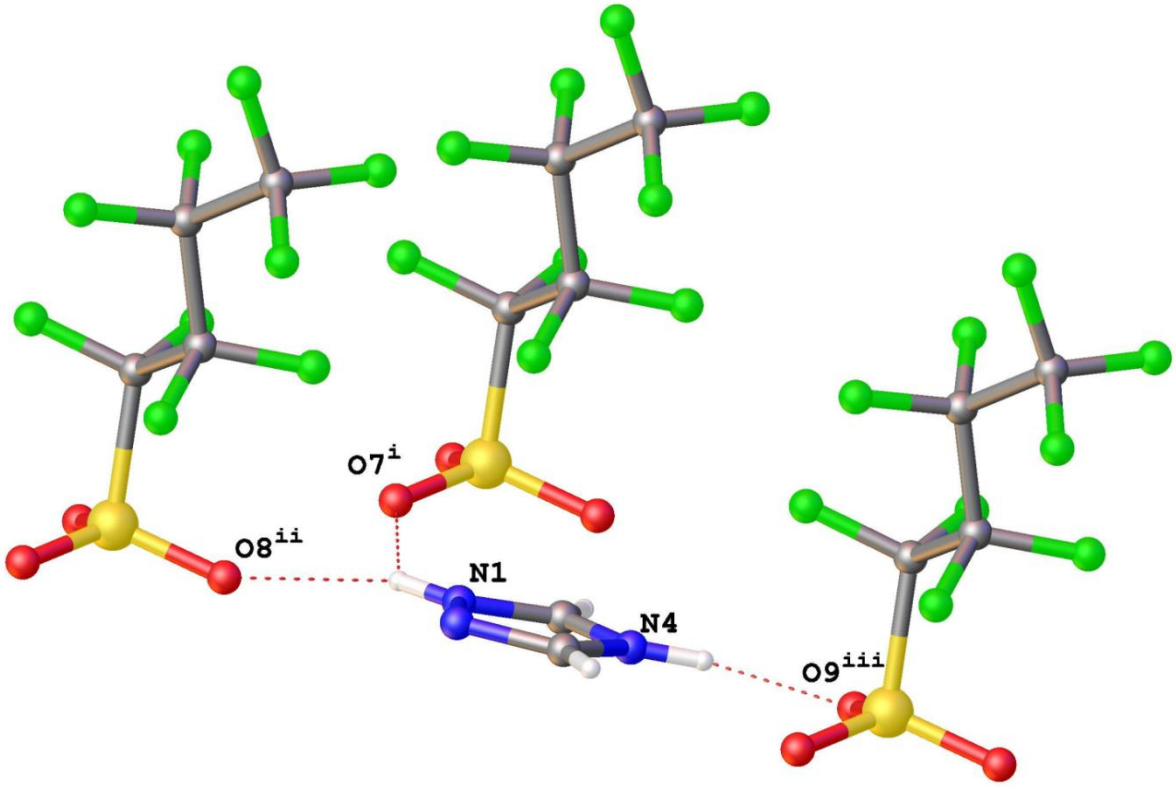

Fig. S11. View of the crystal structure of **1** at −173 °C showing the hydrogen bonds between one 1,2,4-triazolium cation and three neighbouring perfluorobutanesulfonate anions (symmetry codes: ^{i} −1+x,−1+y,z; ^{ii} x,−1+y,z; ^{iii} −1+x,y,z).

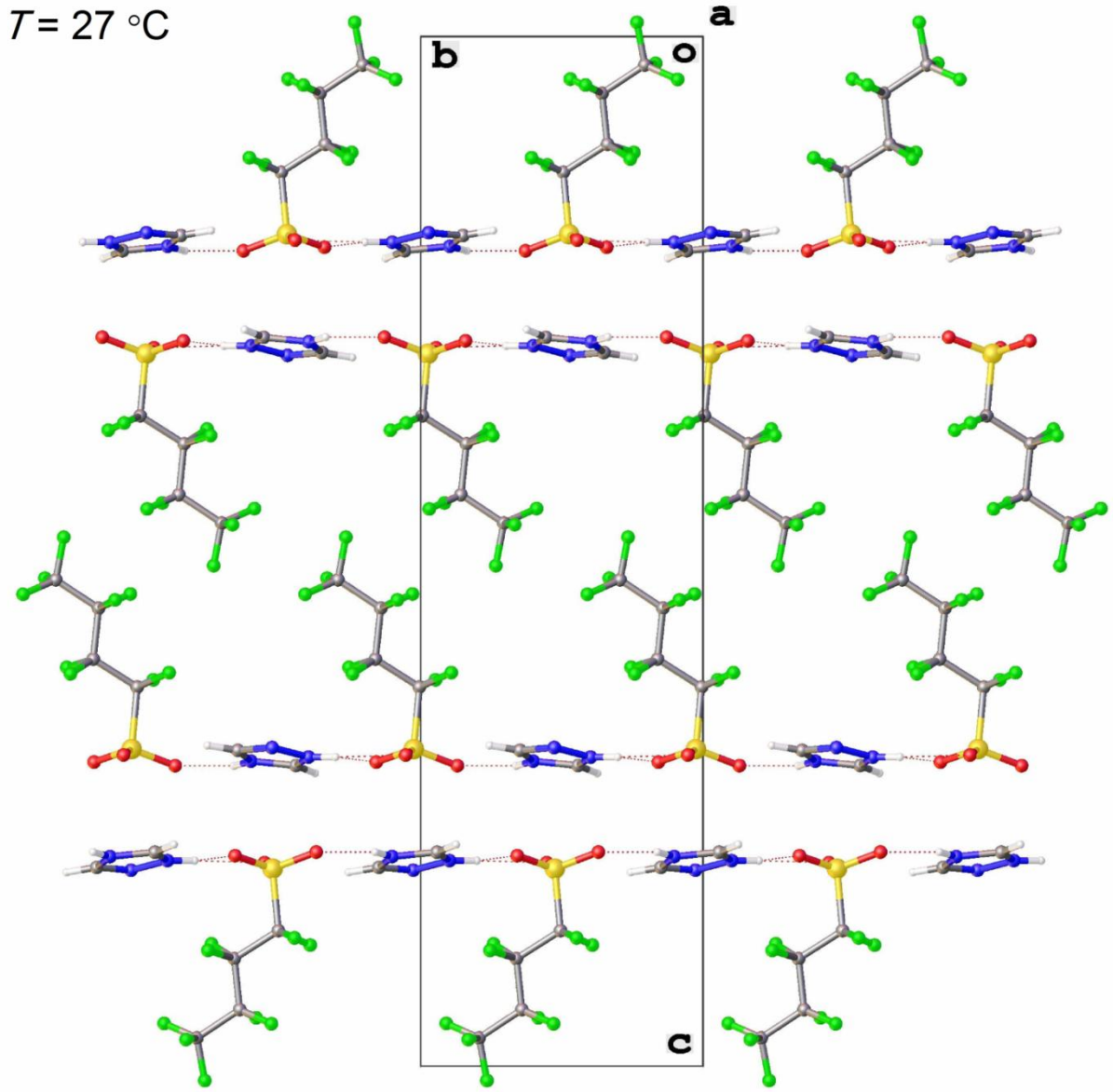

Fig. S12. View of the packing in the crystal structure of **1** at 27 ℃ (C: grey; H: white; F: green; N: blue; O: red; S: yellow).

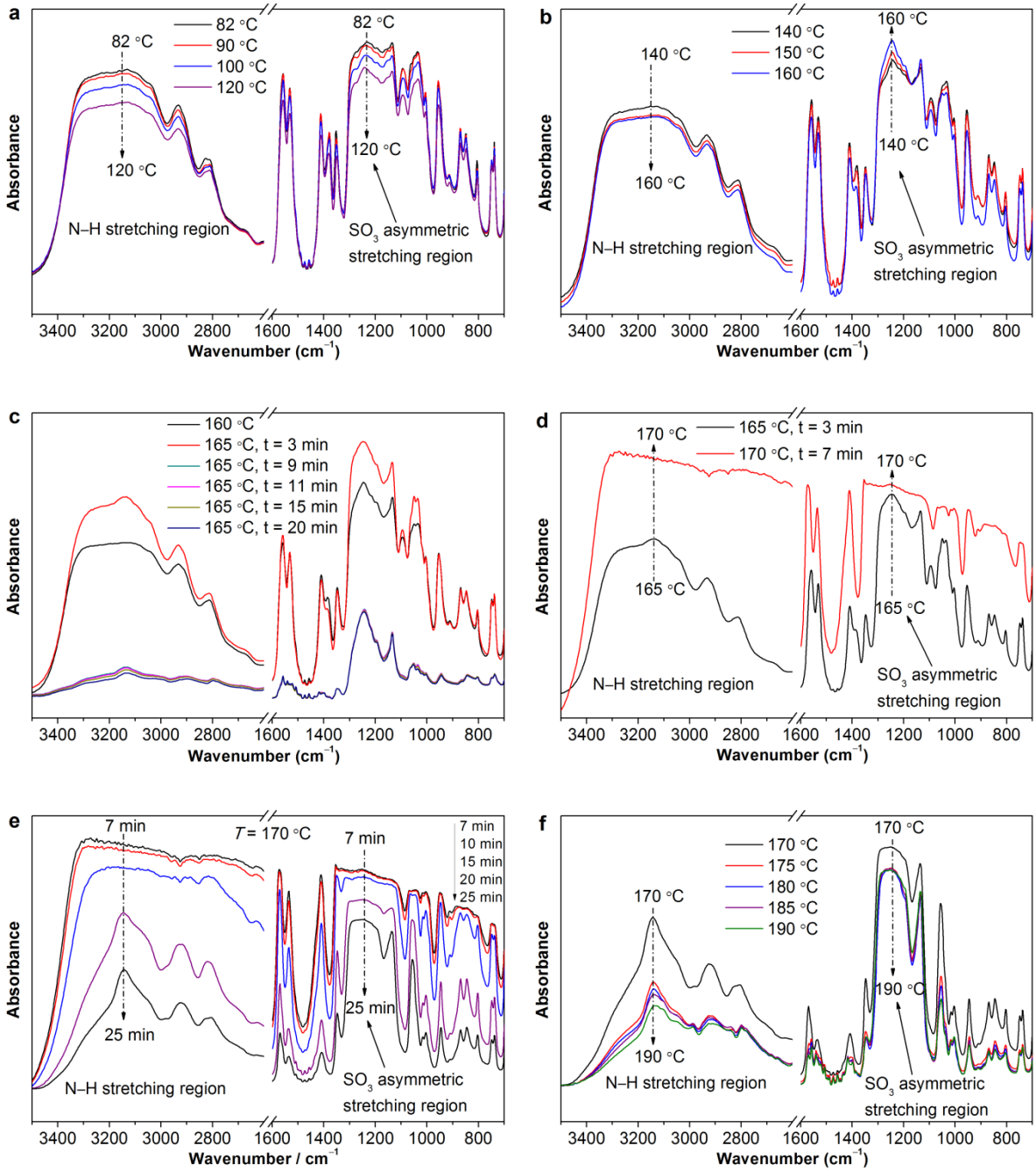

Fig. S13. Variable-temperature FT-IR spectra of **1** in the temperature range of 82−190 ℃: (a) 82−120 ℃; (b) 140−160 ℃; (c) the evolution of the IR spectrum of the sample when the temperature reached 165 ℃ for 3, 9, 11, 15, and 20 min; (d) the IR spectra of the sample when it was heated at 165 and 170 ℃ for 3 and 7 min, respectively; (e) the evolution of the IR spectrum of the sample when the temperature reached 170 ℃ for 7, 10, 15, 20 and 25 min; (f) 170−190 ℃. The sample was thermally equilibrated at each temperature for at least 15 min (unless otherwise specified) prior to the measurements. The heating rate was 1 ℃ min^{-1} between two consecutive temperatures. Note that the IR spectra of the crystal of **1** at temperatures ≤ 160 ℃ were stable and did not change with time. As from 165 °, the sample was no longer a single crystal (**Fig. S17** and **S18**).

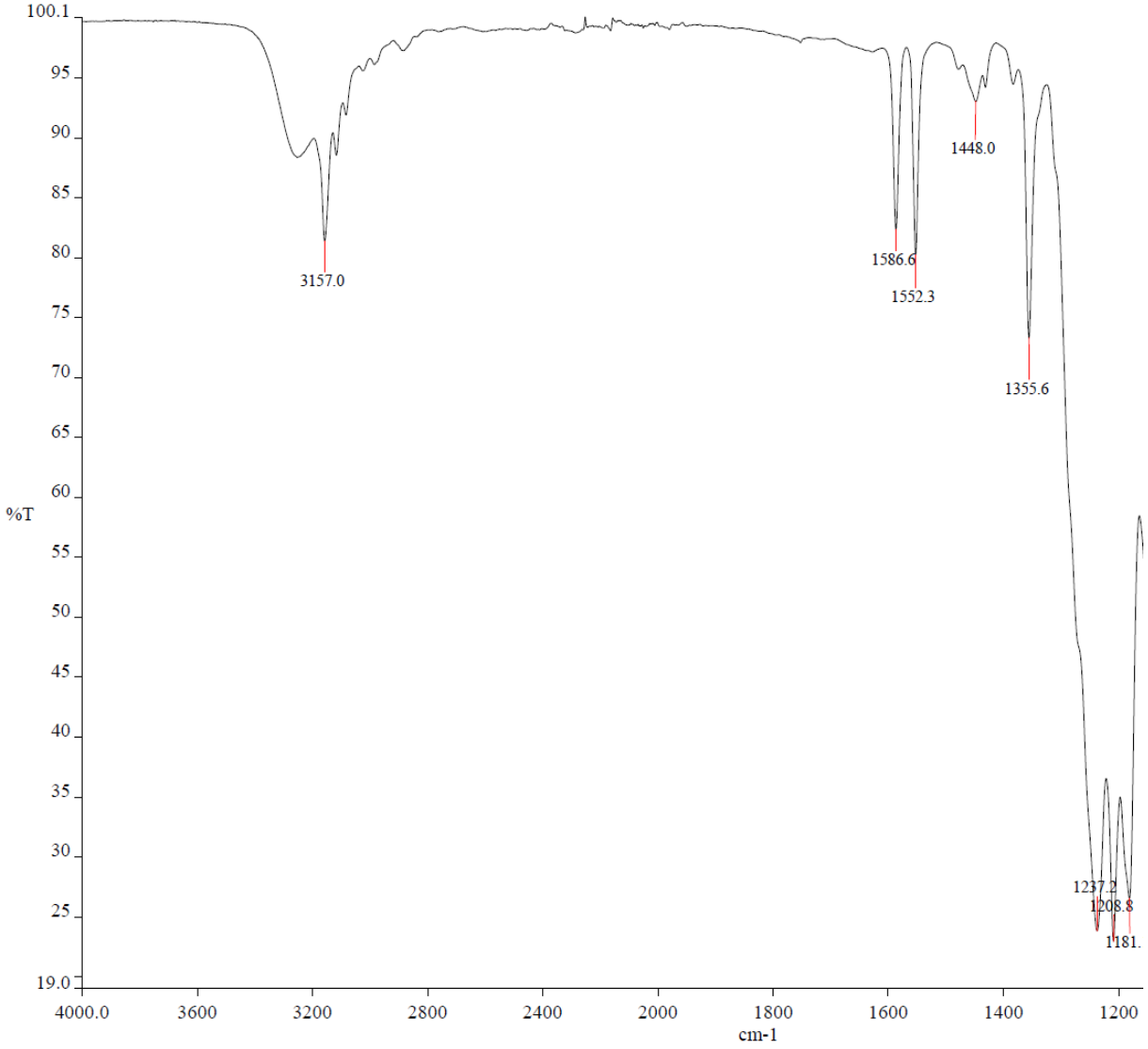

Fig. S14. FT-IR spectrum of 1-methylimidazolium perfluorobutanesulfonate at room temperature without exhibiting sharp vibrational modes at around 1419 and 1396 cm^{-1}.[S26]

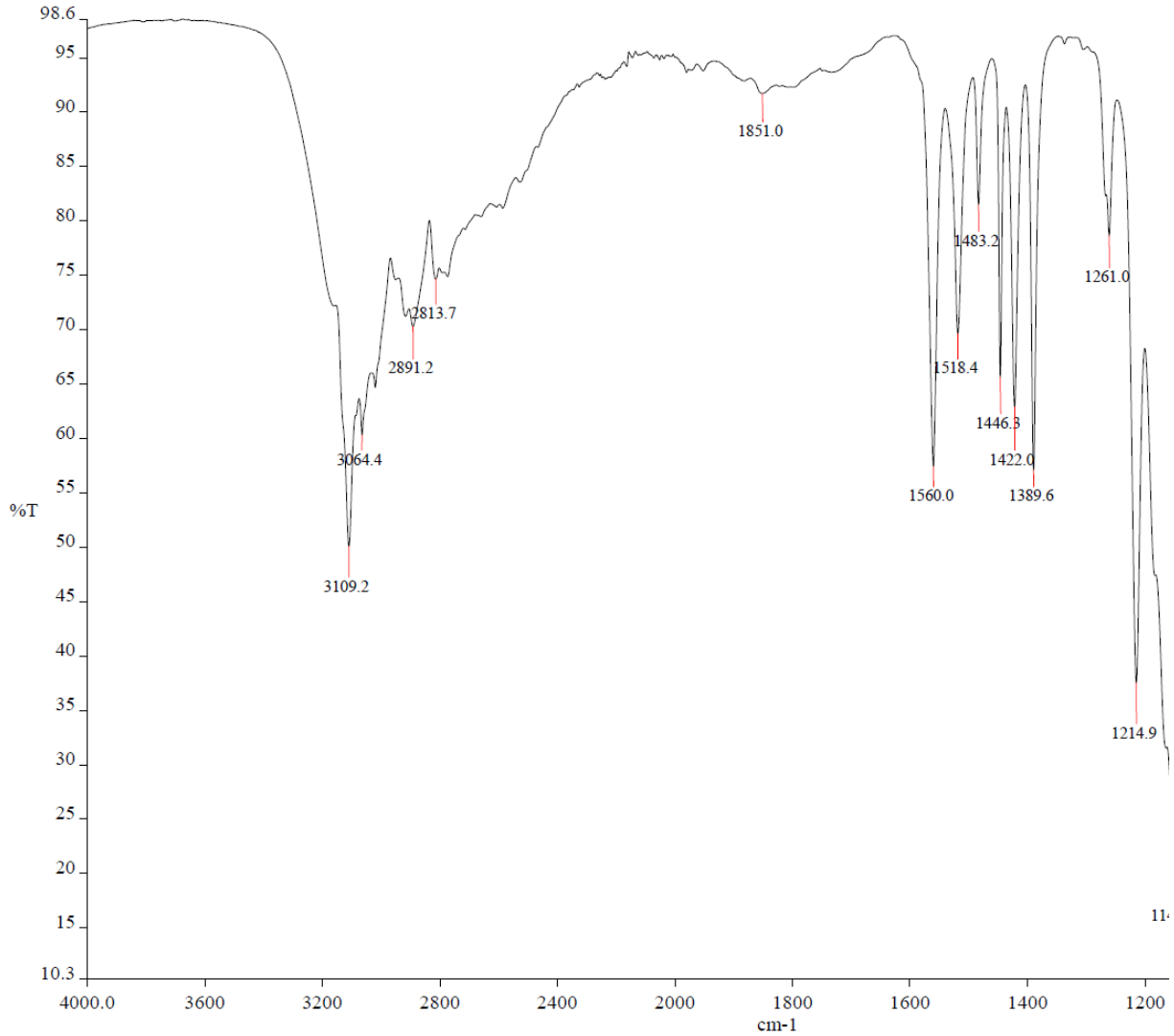

Fig. S15. FT-IR spectrum of 1,2,4-triazolium benzenesulfonate at room temperature, showing sharp vibrational frequencies at 1422 and 1390 cm^{-1}.[S26]

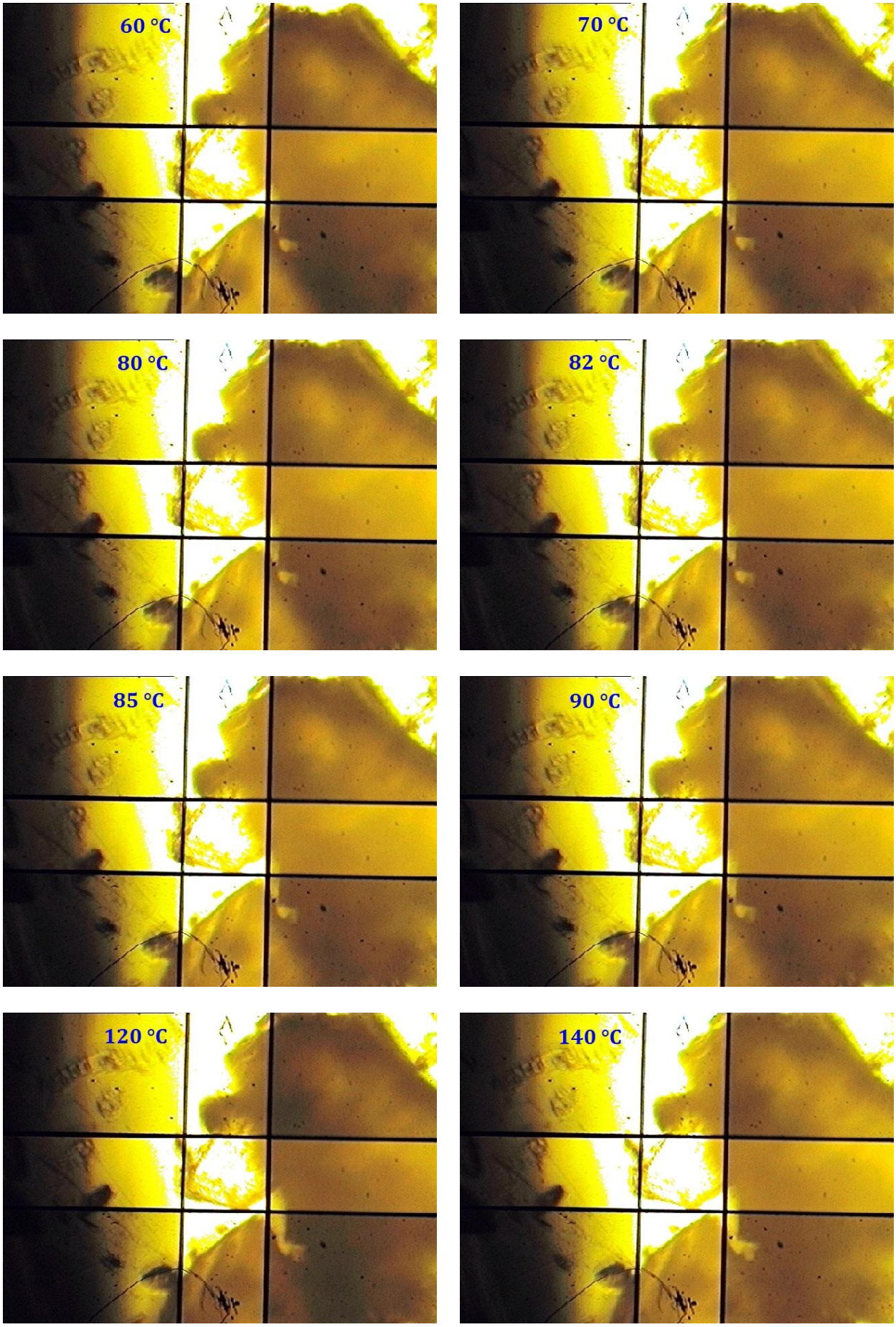
60 °C
70 °C
80 °C
82 °C
85 °C
90 °C
120 °C
140 °C

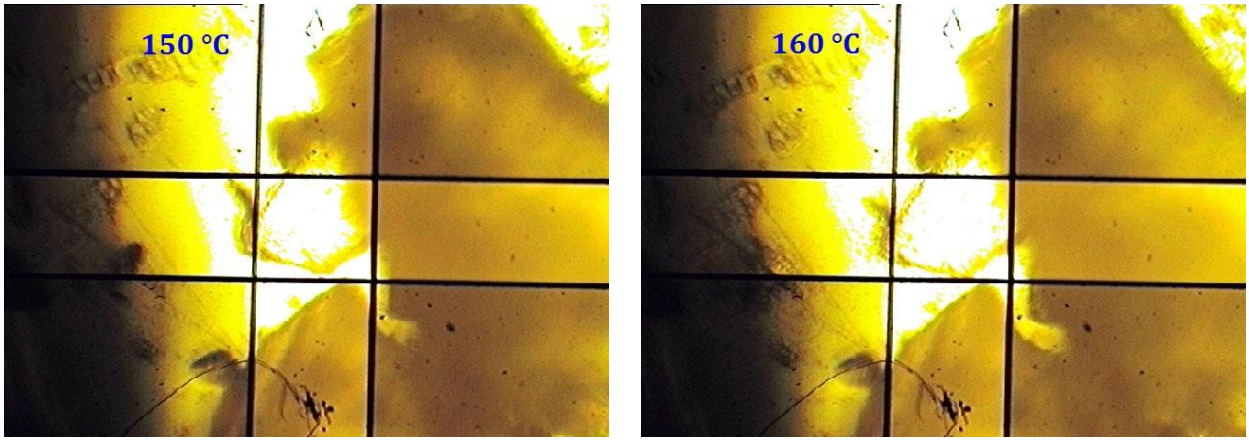

Fig. S16. Images of the single crystal recorded during variable-temperature FT-IR measurements at 60, 70, 80, 82, 85, 90, 120, 140, 150 and 160 ℃, respectively. From 28 ℃ to 70 ℃, the heating rate was 5 ℃ min^{-1} between two consecutive temperatures and was adjusted to 1 ℃ min^{-1} from 70 ℃ onwards. The sample was thermally equilibrated at each temperature for at least 15 min prior to the measurements. Images were taken by using the FT-IR imaging microscope (with a 15× objective lens) of Varian 670-IR FT-IR spectrometer. The crystal was in the central square.

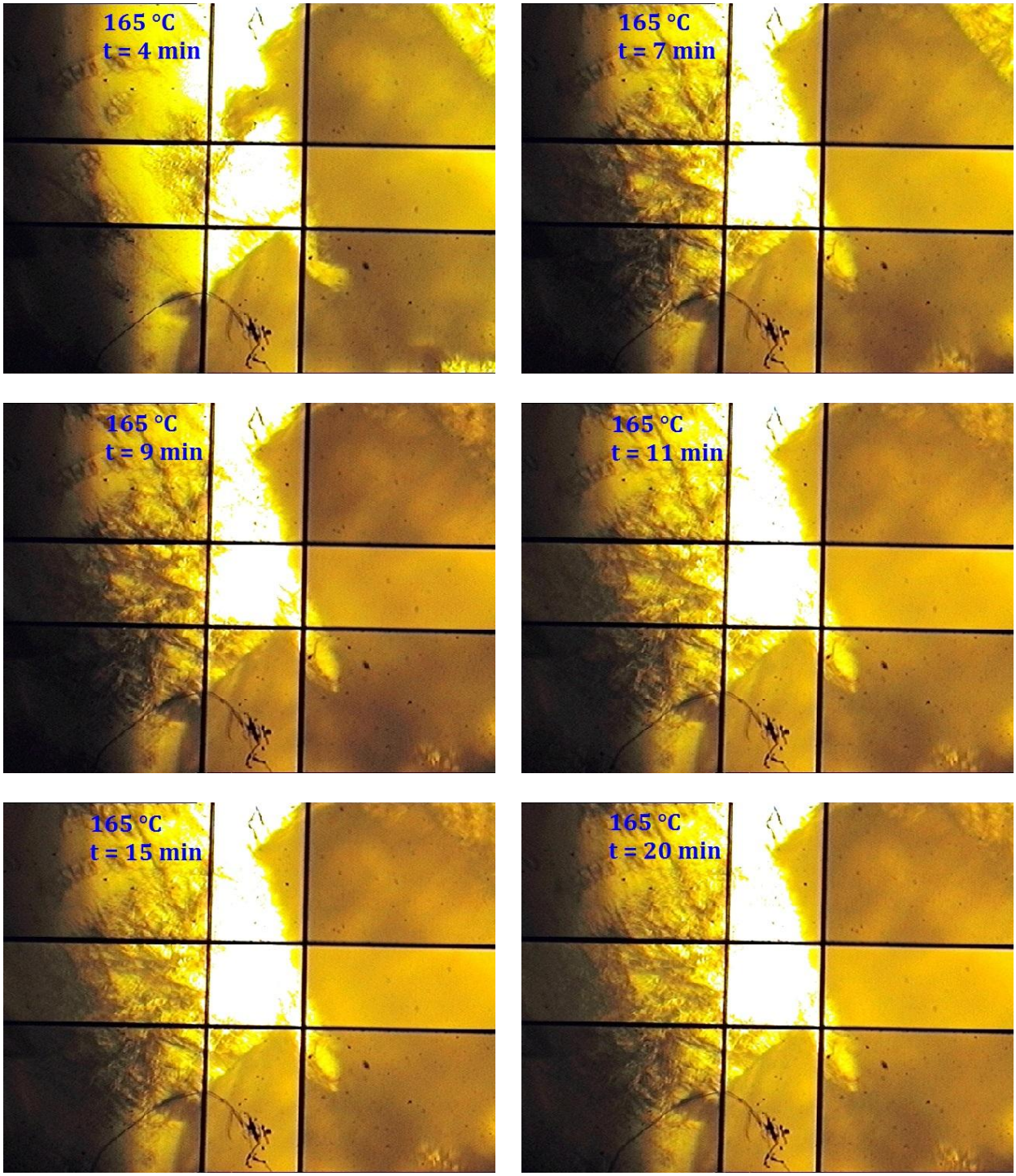

Fig. S17. The evolution of the optical microscopic images of the sample when the temperature reached 165 ℃ for 4, 7, 9, 11, 15, and 20 min. Images were taken by using the FT-IR imaging microscope (with a 15× objective lens) of Varian 670-IR FT-IR spectrometer. The sample, which was a crystal in the central square at the beginning, spreaded to its surroundings as if it flows. Together with Movie S1 showing the dynamic changes of the crystal of **1** heated at 165 ℃, the morphological changes upon heating from 160 ℃ to 165 ℃ may indicate a thermal-induced plastic flow. The seemingly "melting" process shown in the supplementary movie (**Movie S1**) is actually not a melting process. The exclusion of the "melting" is supported by the DSC (**Fig. 3**, **Fig. S6** and **S7**) and temperature-dependent powder XRD (**Fig. S18**) measurements for **1** as well as visual observations for a bulk sample of **1** during heating.

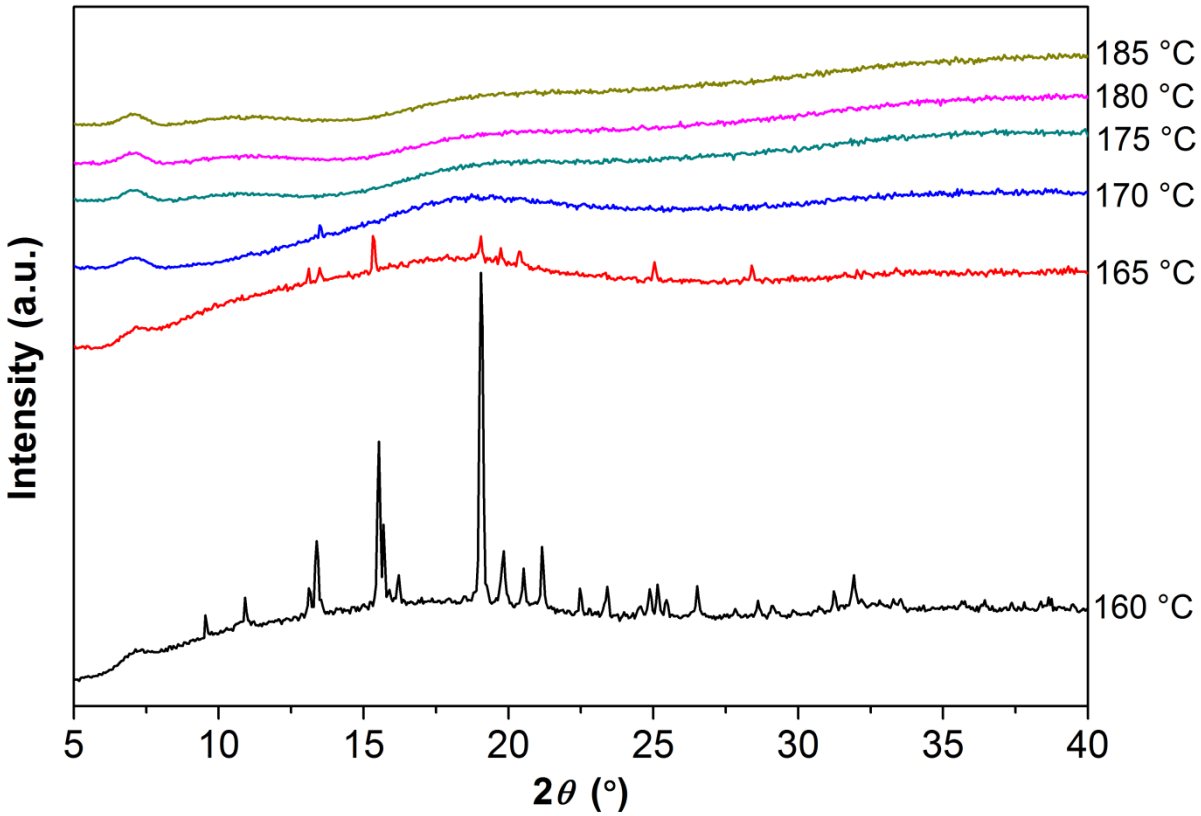

Fig. S18. Temperature-dependent powder XRD patterns of powders of **1** from 160 ℃ to 185 ℃ in an argon atmosphere. *The powders were used as synthesized (after purification) without being further ground into fine powders.* The sample was stabilized at each measurement temperature (accuracy: ±1 ℃) for about 20 min prior to the measurement. The temperature ramp between two consecutive temperatures was 5 ℃ min^{-1}. Measurements were carried out on a powder X-ray diffractometer (X'Pert PRO, PANalytical) using Cu Kα radiation (λ = 1.5406 Å). Each measurement consisted of a θ–2θ scan from 5 ° to 60 ° with a step size of 0.052 ° and a scan speed of 0.048 ° s^{-1}. Clearly, the sample began to lose its crystallinity at 165 ℃. At temperatures ≥ 170 ℃, it can be considered to be an amorphous material, implying the greatly increased disorder. Note that **1** melts at around 181 ℃. Importantly, visual observation confirms that **1** is still solid before 181 ℃.

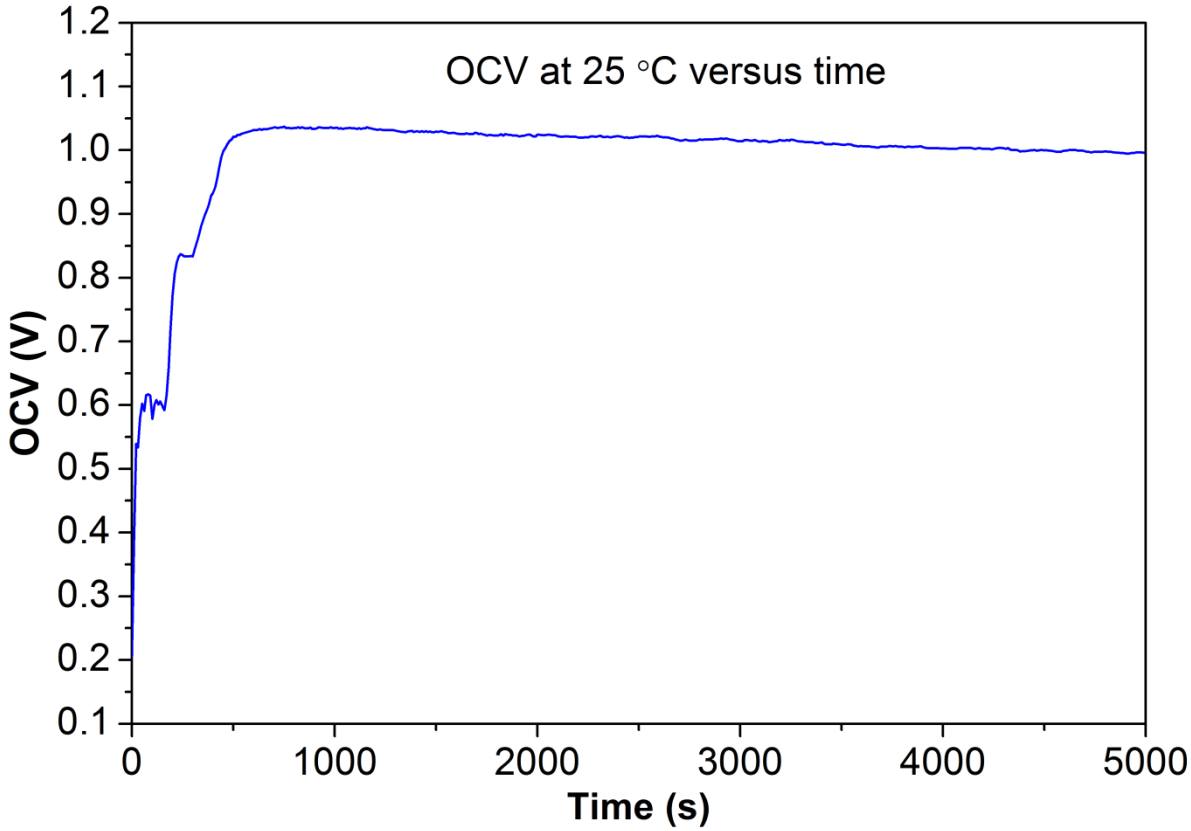

Fig. S19. OCV at 25 ℃ versus time evaluated using the following electrochemical cell: H_2, Pt/C|pressed pellet of powders of **1**|Pt/C, air. The gases were both dry. *The powders were used as synthesized (after purification) without being further ground into fine powders.* The fact that the OCV values were almost constant over 4000 seconds demonstrates the stability of the material in the dry hydrogen/air fuel cell environments. It should be noted that after grinding into fine powders, better OCV profiles are expected as evidenced in **Fig. 14b**, which is likely due to the resulting denser pellet as the elelectrolyte for fuel cells.

Section 4: Supplementary Table

Table S1. Fitting slopes of the polarization curves shown in Fig. 14a.

T/ ℃	Slope/(MΩ cm^2)[a]	R^2 [b]	σ/(S cm^{-1})[c]
120	0.31262	0.958	3.1988×10^{-7}
130	0.17139	0.99021	5.8346×10^{-7}
140	0.09599	0.99658	1.0418×10^{-6}
150	0.05885	0.99886	1.6992×10^{-6}
160	0.05267	0.99698	1.8986×10^{-6}
170	0.05209	0.99929	1.9198×10^{-6}
180	0.01097	0.99806	9.1158×10^{-6}

[a] Slope = resistance × area, where area = 0.5 cm^2. [b] R^2: correlation coefficient. [c] $\sigma = d$/slope, where the thickness, *d*, of the cylindrical pellet is 0.10 cm.

We show that the direct current (DC) ionic conductivity of the pellet of the material in an operating fuel cell determined from the polarization curve agrees well with the alternating current (AC) ionic conductivity for a similar pellet of the POIPC **1**. This may be considered as additional proof that the material has significant proton conductivity, so that protonic conductivity constitutes the majority of the ionic conductivity in the lower plateau region (phase I, 100−155 °C). The reasons are explained as follows:

(a) Qualitatively, the very high open circuit voltage (OCV) (as high as 1.05 V at 150 ℃) of our POIPC material provides evidence of long-range proton conduction. If we look at the principle of fuel cells, proton transfers across the "membrane" between anode and cathode is a vital process for the operating of fuel cells. As the OCV is high (approaching the theoretical value), that means the fuel cell reactions happen with long-range proton transfers from the anode to the cathode to complete the net reaction of "H_2 + 1/2 $O_2 \rightarrow H_2O$". As the perfluorobutanesulfonate anions are unlikely to contribute to the current during fuel cell operation, the current should be contributed by the cations. No matter whether the cations move with 1,2,4-triazole as a vehicle for protons (vehicle mechanism), or the protons themselves hop (Grotthuss mechanism or structural diffusion), they both result in proton conduction. Hence, high OCV values are strong evidence of protonic conductivity and protons (including 1,2,4-triazolium cations) as the conducting species.

(b) It is well know that there are typically three factors influencing the fuel cell polarization curves: kinetic loss, ohmic loss (cell resistance), and mass transport loss.[S27] During the fuel cell test, the polarization curves were measured from 120 ℃ to 180 ℃ by linear sweep voltammetry at a scan rate of 10 mV s^{-1}, using the following electrochemical cell: H_2, Pt/C|cylindrical dense pellet of compound **1**|Pt/C, air. The pellet had a diameter of 13 mm and a thickness of 1.0 mm. As the electrodes are gas diffusion electrodes and the current densities are very low, the mass transport can be neglected. From the low AC ionic conductivity (Fig. 11), we know that the resistance of the pellet as a thin film electrolyte constitutes the absolute majority part of the cell resistance (pellet, anodes, cathodes, lines and so on). While the resistance of the 1.0 mm thick pellet can be as high as a few tenths of mega ohm, even the electrochemical reaction resistance (*i.e.* charge transfer resistance R_{ct}, which contributes to the kinetic loss) can be neglected when we consider the large resistance of the pellet film and the high open circuit voltage of the single fuel cells. Therefore, we may approximately estimate the DC ionic conductivity from the slopes of the polarization curves as shown in Fig. 14a and Table S1. It was then found that the obtained DC ionic conductivity agrees well with the AC ionic conductivity for a similar pellet of the material, confirming the dominate proton conductivity of the material.

Section 5: Supplementary Movie

Movie S1. The plastic flow of a crystal at t = ~3 min when it was heated at 165 ℃.

References

[S1] J. Luo, J. Hu, W. Saak, R. Beckhaus, G. Wittstock, I. F. J. Vankelecom, C. Agert and O. Conrad, *J. Mater. Chem.*, 2011, **21**, 10426.

[S2] J. Luo, T. V. Tan, O. Conrad and I. F. J. Vankelecom, *Phys. Chem. Chem. Phys.*, 2012, **14**, 11441.

[S3] J.-B. Brubach, A. Mermet, A. Filabozzi, A. Gerschel and P. Roy, *J. Chem. Phys.*, 2005, **122**, 184509.

[S4] E. S. Stoyanov, K. C. Kim and C. A. Reed, *J. Am. Chem. Soc.*, 2006, **128**, 8500.

[S5] M. S. Miran, H. Kinoshita, T. Yasuda, M. A. B. H. Susan and M. Watanabe, *Chem. Commun.*, 2011, **47**, 12676.

[S6] D. Bougeard, N. Le Calvé, B. Saint Roch and A. Novak, *J. Chem. Phys.*, 1976, **64**, 5152.

[S7] A. Bernson and J. Lindgren, *Solid State Ionics*, 1993, **60**, 37.

[S8] J. Luo, O. Conrad and I. F. J. Vankelecom, *J. Mater. Chem.*, 2012, **22**, 20574.

[S9] R. Langner and G. Zundel, *J. Chem. Soc., Faraday Trans.*, 1998, **94**, 1805.

[S10] C. M. Burba, N. M. Rocher, R. Frech and D. R. Powell, *J. Phys. Chem. B*, **2008**, **112**, 2991.

[S11] S. A. Forsyth, K. J. Fraser, P. C. Howlett, D. R. MacFarlane and M. Forsyth, *Green Chem.*, 2006, **8**, 256.

[S12] K. Kuchitsu, H. Ono, S. Ishimaru, R. Ikeda and H. Ishida, *Phys. Chem. Chem. Phys.*, 2000, **2**, 3883.

[S13] N. G. Parsonage and L. A. K. Staveley, *Disorder in Crystals*, Clarendon Press, Oxford, 1978.

[S14] J. Luo, O. Conrad and I. F. J. Vankelecom, *J. Mater. Chem. A*, 2013, **1**, 2238.

[S15] W. A. Henderson, V. G. Young, Jr., W. Pearson, S. Passerini, H. C. De Long and P. C. Trulove, *J. Phys.: Condens. Matter*, 2006, **18**, 10377.

[S16] F. Meersman, B. Geukens, M. Wübbenhorst, J. Leys, S. Napolitano, Y. Filinchuk, G. Van Assche, B. Van Mele and E. Nies, *J. Phys. Chem. B*, 2010, **114**, 13944.

[S17] P. Szklarz, A. Pietraszko, R. Jakubas, G. Bator, P. Zieliński and M. Gałazka, *J. Phys.: Condens. Matter*, 2008, **20**, 255221.

[S18] W. A. Henderson, D. M. Seo, Q. Zhou, P. D. Boyle, J.-H. Shin, H. C. De Long, P. C. Trulove and S. Passerini, *Adv. Energy Mater.*, 2012, **2,** 1343.

[S19] J. M. Chezeau and J. H. Strange, *Phys. Rep.*, 1979, **53**, 1.

[S20] J. Sun, D. R. MacFarlane and M. Forsyth, *Solid State Ionics*, 2002, **148**, 145.

[S21] R. Asayama, J. Kawamura and T. Hattori, *Chem. Phys. Lett.*, 2005, **414**, 87.

[S22] T. Enomoto, S. Kanematsu, K. Tsunashima, K. Matsumoto and R. Hagiwara, *Phys. Chem. Chem. Phys.*, 2011, **13**, 12536.

[S23] R. Taniki, K. Matsumoto, R. Hagiwara, K. Hachiya, T. Morinaga and T. Sato, *J. Phys. Chem. B*, 2013, **117**, 955.

[S24] D. R. MacFarlane and M. Forsyth, *Adv. Mater.*, 2001, **13**, 957.

[S25] J. Efthimiadis, S. J Pas, M. Forsyth and D. R. MacFarlane, *Solid State Ionics*, 2002, **154−155**, 279.

[S26] J. Luo, unpublished data, **2011**.

[S27] M. K. Debe, *Nature*, 2012, **486**, 43.